

Cite this: *J. Mater. Chem. A*, 2019, 7, 15782

# Constructing Z-scheme SnO<sub>2</sub>/N-doped carbon quantum dots/ZnSn(OH)<sub>6</sub> nano hybrids with high redox ability for NO<sub>x</sub> removal under VIS-NIR light†

Yanfeng Lu,<sup>abd</sup> Yu Huang,<sup>id</sup>\*<sup>abc</sup> Jun-ji Cao,<sup>abc</sup> Haiwei Li,<sup>id</sup><sup>e</sup> Wingkei Ho<sup>f</sup> and Shun Cheng Lee<sup>e</sup>

Photocatalysts with a wide optical response range and high oxidation ability are essential for their application in air pollution control. In this study, mesoporous SnO<sub>2</sub>/NCDs/ZnSn(OH)<sub>6</sub> (NCDs = N-doped carbon quantum dots) Z-scheme nano hybrids were synthesized for the first time using an *in situ* strategy. The ternary Z-scheme catalysts showed significantly enhanced visible and near-infrared light-driven photocatalytic activities for nitric oxide (NO) removal (37%), while the toxic nitrogen dioxide (NO<sub>2</sub>) intermediate was suppressed completely. The Z-schematic transfer mechanism was confirmed through characterizing the intrinsic properties of the as-prepared sample. The NCDs, as an electron transport bridge, improve both the broad-spectrum light-harvesting ability and the rapid separation of photoinduced electrons. Compared with the binary counterparts, the SnO<sub>2</sub>/NCDs/ZnSn(OH)<sub>6</sub> ternary nano hybrid can generate more reactive oxygen-containing radicals during the photocatalytic reaction, owing to its ability to supply sufficient free surface OH. This study provides insights into the heterogeneous photocatalytic Z-scheme reaction mechanism.

Received 2nd April 2019

Accepted 3rd June 2019

DOI: 10.1039/c9ta03504d

rsc.li/materials-a

## 1. Introduction

Photocatalysis is a promising and economically feasible technology to control air pollution.<sup>1,2</sup> Previous studies showed that photocatalysis can effectively remove NO<sub>x</sub>, which are among the precursors for secondary aerosol and acid rain formation.<sup>3</sup> However, the efficiency of photocatalytic NO<sub>x</sub> removal is strongly affected by the optical absorption range, charge separation efficiency, and redox capacity of photocatalysts.<sup>4</sup> Further, it is difficult for a single-component photocatalyst to resolve all these problems. For example, metal/nonmetal doping can extend the visible light absorption range of TiO<sub>2</sub>, but this may not guarantee significant improvement of photocatalytic activity because the efficiency of a photocatalyst is also affected

by charge separation and redox ability.<sup>5,6</sup> Therefore, it is necessary to explore nano hybrids with an appropriate wide optical absorption range with high interfacial charge transfer rate and strong redox capability, in order to achieve photocatalytic NO<sub>x</sub> removal.

ZnSn(OH)<sub>6</sub> (ZHS), a non-toxic perovskite hydroxide having a face-centered-cubic crystal structure filled with OH groups on the surface, has high photocatalytic activity under UV light irradiation.<sup>7,8</sup> It is widely applied in gas sensors,<sup>9</sup> antibacterial materials<sup>10</sup> and lithium-ion batteries.<sup>11</sup> It is also used as a photocatalyst for pollutant removal, showing higher conversion and mineralization for benzene, phenol and dyes.<sup>12–15</sup> Recently, various heterojunction photocatalysts such as Au/ZHS,<sup>16</sup> ZHS-GO<sup>17</sup> and BiOI/ZHS<sup>18</sup> have been constructed to improve the optical absorption and enhance the quantum yield of ZHS. Most of them employed two-step synthesis strategies for preparing the ZHS-based heterojunction structures. However, this approach could not easily achieve uniform structure and it also increased the resistance against interfacial electron transport. It was reported that an *in situ* strategy for fabricating the α-Bi<sub>2</sub>O<sub>3</sub>/(BiO)<sub>2</sub>CO<sub>3</sub> heterojunction with well-defined morphologies can simultaneously extend the light absorption to the visible region and promote quick charge-carrier migration driven by the strong innate electric field at the hetero-interface.<sup>19</sup> This strategy can efficiently lower the interfacial transfer barrier for electron migration. Thus, constructing heterojunction structures with homogeneous distribution of components by an *in situ* strategy is an effective way to prepare new nano hybrid

<sup>a</sup>Key Laboratory of Aerosol Chemistry and Physics, Institute of Earth Environment, Chinese Academy of Sciences, Xi'an 710061, China. E-mail: huangyu@ieecas.cn; Fax: +86-2962336261; Tel: +86-2962336261

<sup>b</sup>State Key Lab of Loess and Quaternary Geology (SKLLQG), Institute of Earth Environment, Chinese Academy of Sciences, Xi'an 710061, China

<sup>c</sup>CAS Center for Excellence in Quaternary Science and Global Change, Xi'an, 710061, China

<sup>d</sup>University of Chinese Academy of Sciences, Beijing 100049, China

<sup>e</sup>Department of Civil and Environmental Engineering, The Hong Kong Polytechnic University, Hung Hom, Hong Kong, China

<sup>f</sup>Department of Science and Environmental Studies, The Hong Kong Institute of Education, Hong Kong, China

† Electronic supplementary information (ESI) available: Experimental and supplementary figures and tables. See DOI: 10.1039/c9ta03504d

materials with excellent properties. In this regard, the SnO<sub>2</sub> semiconductor, as an appropriate cocatalyst with a narrow-band-gap semiconductor, can act as a favorable candidate for building homogeneous nanostructures on ZHS nanocubes. Most importantly, a synergistic effect between SnO<sub>2</sub> and ZHS facilitating the formation of active oxygen radicals accounts for the high performance of benzene degradation under UV irradiation.<sup>7</sup> However, even with so many structural and performance advantages, both the solar energy conversion efficiency and the quantum efficiency of pure ZHS or binary SnO<sub>2</sub>/ZHS nanocomposites are still low for practical applications due to the sluggish transfer of photo-generated carriers and the weakened redox abilities of electrons and holes.

Using Z-scheme-type photocatalysts is a highly effective approach to promote charge separation and enhance the reduction/oxidation abilities on different active sites.<sup>20,21</sup> Previous studies have revealed that Z-scheme composites can retain photogenerated charges with stronger redox capability separately on semiconductors, in order to thoroughly oxidize pollutants.<sup>22,23</sup> Ga-LTCA/Au/BiVO<sub>4</sub> sheets were reported as a promising photocatalyst for Z-scheme water splitting.<sup>24</sup> The noble metal layer as the mediator is crucial for efficient charge transfer between the BiVO<sub>4</sub> and LTCA, eventually enhancing the water-splitting activity. Instead of precious metals, a similar function can be achieved in the Z-scheme system by N-doped carbon quantum dots (NCDs). As a nontoxic and low-cost carbon species, NCDs have excellent electron transfer and storage properties and unique up-conversion fluorescence ability.<sup>25,26</sup> Combining NCDs with rutile TiO<sub>2</sub> to form TiO<sub>2</sub>/NCDs composites can allow the photogenerated electrons to transfer more efficiently to the conduction band (CB) of TiO<sub>2</sub> and convert into other reactive oxidative species.<sup>25</sup> The up-conversion fluorescence properties of NCDs and efficient charge separation led to their enhanced photocatalytic performance.<sup>26,27</sup> So, NCDs are a suitable candidate for constructing Z-scheme-type structures.

Motivated by the above considerations, in this work we report a Z-scheme mesoporous SnO<sub>2</sub>/NCDs/ZHS ternary nanohybrid prepared through a rational design and *in situ* self-assembly synthesis. The morphology, composition, and optical and electrochemical properties of the prepared photocatalysts were analyzed comprehensively. The wide light-absorption range and the spatial distribution characteristics of surface electrons were modulated by the SnO<sub>2</sub>/NCDs/ZHS ternary nanohybrid photocatalyst. The results indicated that the mesoporous SnO<sub>2</sub>/NCDs/ZHS Z-scheme nanohybrids displayed excellent activity and stability for photocatalytic removal of NO under visible and near-infrared light (VIS-NIR) irradiation. In addition, the experimentally proven specific structural characteristics and strong redox ability led to the complete inhibition of toxic NO<sub>2</sub> intermediates.

## 2. Experimental section

### 2.1 Synthesis of SnO<sub>2</sub>/NCDs/ZnSn(OH)<sub>6</sub> nanohybrids

All chemicals were of analytical grade and used directly without further purification. The ternary nanohybrid SnO<sub>2</sub>/NCDs/

ZnSn(OH)<sub>6</sub> (SnO<sub>2</sub>/NCDs/ZHS) was produced by a simple *in situ* solvothermal method (Scheme S1†). SnCl<sub>4</sub>·5H<sub>2</sub>O (98%, Sigma-Aldrich, 0.7 g) and NaOH (96.0%, Sinopharm Chemical Reagent Co., Ltd., 0.4 g) were first dissolved in 15 mL deionized water and stirred for 30 min. Then, (CH<sub>3</sub>COO)<sub>2</sub>Zn·2H<sub>2</sub>O (98%, Sigma-Aldrich, 0.4 g) was dispersed in 20 mL ethanol under ultrasound for 30 min, and the resultant mixture was added dropwise into the first solution. The mixture was kept stirring for 7 h and the pH was maintained at 6.1 using sodium hydroxide solution (2 M). Subsequently, 0.6 mL (volume ratio: 1.7%) of fresh NCDs solution was added into the above solution, stirred for 1 h, and then transferred to a 50 mL Teflon-lined stainless steel autoclave and maintained at 160 °C for 12 h. The resulting composite was washed with ethanol and water three times, and dried at 60 °C for 12 h to obtain the SnO<sub>2</sub>/NCDs/ZHS sample.

All reference samples were prepared by a similar solvothermal method. To obtain the pure ZHS, the mixture pH was adjusted to 13.1 using sodium hydroxide solution (5 M). The NCDs/ZnSn(OH)<sub>6</sub> (NCDs/ZHS) was synthesized by adding 0.6 mL (volume ratios: 1.7%) of fresh NCD solution and the solution pH was kept at 13.1. The SnO<sub>2</sub>/ZnSn(OH)<sub>6</sub> (SnO<sub>2</sub>/ZHS) sample was synthesized by maintaining the mixture pH at 6.1 with the same solvothermal method but without the NCD precursor.

### 2.2 Characterization

Crystallographic information was obtained from X-ray diffraction (XRD; PANalytical, X'pert, Netherlands) patterns using Cu Kα (λ = 1.5406 Å) radiation. Raman spectra were recorded on a Laser Confocal Micro-Raman Spectrometer (LabRAM HR800, France). UV-Vis diffuse reflectance spectra were recorded using a Varian Cary 100 Scan UV-Visible system (DRS, Agilent Corp., USA) using Ba<sub>2</sub>SO<sub>4</sub> reflection as a reference. The sample morphology and structure were characterized by high-resolution transmission electron microscopy (TEM, JEOL JEM-3010, Japan). The surface chemical states were investigated by X-ray photoelectron spectroscopy (XPS, Thermo Escalab 250Xi, USA) using a 532 nm YAG laser as the excitation source. Photoluminescence (PL) spectra were recorded with a fluorescence spectrophotometer (FLS-980, Edinburgh Instrument Ltd., England). The Brunauer–Emmett–Teller surface area and pore structure of the as-prepared samples were obtained from the adsorption branch of the isotherms and Barrett–Joyner–Halenda formula at 77 K (BET, Gemini VII 2390, Micromeritics Instrument Corp., Norcross, GA, USA). The light source-monochromator-lock-in surface photovoltage spectroscopy (SPS) detection system consists of a monochromatic light source with a 500 W xenon lamp through a triple-prism monochromator (Hilger and Watt, D300), an amplifier (Brookdeal, 9503-SC) with a light chopper, a photovoltaic cell and a computer. All the SPS tests were performed at room temperature with an ITO electrode film. A JES-FA200 instrument was used to record electron spin resonance (ESR) signals to detect free radicals in the sample, after mixing the as-prepared samples with 5,5'-dimethyl-1-pyrroline-N-oxide (DMPO) solution.

### 2.3 *In situ* DRIFTS investigation of photocatalytic NO oxidation intermediates

The diffuse reflectance infrared spectrum (DRIFTS) was recorded on a VERTEX 70 FTIR spectrometer (Bruker, Germany) equipped with an *in situ* diffuse reflectance cell (Harrick), light source, pretreatment equipment and a high-sensitivity mercury cadmium telluride (MCT) detector cooled by liquid N<sub>2</sub> (Scheme S2†). The samples were purged with high-purity He for 1 h at 150 °C to clean the catalyst surface and cooled to room temperature (30 °C) for background measurement. Then, the reaction gas containing 30 mL min<sup>-1</sup> NO (100 ppm) and 30 mL min<sup>-1</sup> O<sub>2</sub> was fed into the reaction chamber. The adsorption and photocatalytic reaction of NO on the catalysts were carried out for 30 min both under dark conditions and under irradiation using a visible light source ( $\geq 420$  nm).

## 3. Results and discussion

### 3.1 Surface structure, chemical composition and morphology of the ternary nanohybrid

Fig. 1a shows the XRD patterns of as-synthesized samples, revealing the presence of cubic phase ZHS (JCPDS no 20-1455) in all samples. Additionally, the high purity of ZHS was confirmed by Raman spectra (Fig. S1†).<sup>28</sup> As shown in the inset of Fig. 1a, the XRD patterns of SnO<sub>2</sub>/ZHS and SnO<sub>2</sub>/NCDs/ZHS display some weak and broad diffraction peaks at  $2\theta = 26.1^\circ$ , indexed to the tetragonal SnO<sub>2</sub> (JCPDS no 77-449) (Fig. S2a and b†).<sup>7</sup> Compared with pristine ZHS, no obvious XRD diffraction peaks of NCDs can be found in the pattern of any samples. However, a new peak at 1598 cm<sup>-1</sup> appeared in the ternary SnO<sub>2</sub>/NCDs/ZHS nanohybrid, confirming that the NCDs were fabricated on the surface.<sup>29</sup> These results demonstrated the successful loading of SnO<sub>2</sub> nanoparticles and NCDs on the surface of ZHS nanocubes. Meanwhile, the surface of SnO<sub>2</sub>/NCDs/ZHS was found to be rich in O–H moieties (Fig. S3†), which was conducive to the production of highly reactive oxygen radicals.<sup>7</sup>

The surface chemical compositions of the SnO<sub>2</sub>/NCDs/ZHS nanohybrids were probed by XPS measurements, which revealed the presence of C, N, O, Sn and Zn (Fig. S4†). The high-resolution spectra of C 1s, located at 284.6 eV, were used to correct the instrument error (Fig. S5†). As shown in Fig. S6a and b,† distinct binding energy drifts were observed in the SnO<sub>2</sub>/NCDs/ZHS nanohybrid, which could be attributed to the formation of a contact interface in the ternary composite, instead of a simple physical mixture. The same phenomenon was observed in the spectra of O 1s (Fig. S7†). Notably, the main peak of the N 1s band was clearly observed in the XPS spectrum for SnO<sub>2</sub>/NCDs/ZHS, which indicated the existence of NCDs on the surface of the catalyst (Fig. 1b).<sup>26</sup> Table S1† summarizes the atomic concentrations of elements in the investigated catalysts. The atomic ratio between SnO<sub>2</sub> and N in SnO<sub>2</sub>/NCDs/ZHS was evaluated as 12% and 3.7%, respectively. These results illustrated the co-existence of SnO<sub>2</sub> and NCDs on the surface of ZHS and the interfacial interaction in the SnO<sub>2</sub>/NCDs/ZHS nanohybrid.

The pristine ZHS particles have a nanocube structure with an edge length of 60–100 nm. They have rich internal pores with high porosity and a dense top surface (Fig. 1c and S8†). The lattice fringe of 0.39 nm corresponds to the (200) plane of ZHS. Notably, the nanocube structure of pristine ZHS was mostly retained in SnO<sub>2</sub>/NCDs/ZHS in terms of the particle size and shape, but the surface became rough in the latter (Fig. 1d). In SnO<sub>2</sub>/NCDs/ZHS, some obvious SnO<sub>2</sub> nanoparticles and NCDs were coated on the surface of ZHS (Fig. 1e). From analyzing the relative crystal lattice space, the edge of ZHS (Fig. 1f) has a lattice space of 0.33 nm, which can be attributed to the (101) plane of SnO<sub>2</sub> nanocrystals.<sup>30</sup> Then, on the surfaces of ZHS and SnO<sub>2</sub>, the crystal lattice space of 0.209 nm corresponded to the (010) plane of NCDs (Fig. 1g and h).<sup>26</sup> The inset of Fig. 1h shows a series of bright spots accompanied by a series of diffraction rings in the selected area electron diffraction (SAED) pattern, which illustrates the polycrystalline nature of the SnO<sub>2</sub>/NCDs/ZHS ternary nanohybrid. Overall, these results demonstrate the co-existence and intimate contact of SnO<sub>2</sub> and NCDs on the ZHS substrate, which greatly facilitates electron transfer.

The dispersion of NCDs and SnO<sub>2</sub> on the catalyst was evaluated by energy dispersive spectroscopy (EDS). The results indicate homogeneous coverage of SnO<sub>2</sub> nanoparticles and NCDs on the surface of ZHS (Fig. 2a–f), which is consistent with the above TEM analyses. The inset table shows that the atomic ratio (%) of Zn/Sn was 23.22/28.09 < 1, which proved the formation of a trace amount of SnO<sub>2</sub> nanoparticles on the surface of ZHS (Fig. 2g). Furthermore, the atomic ratio of N was 7.94%, corresponding to the numerous NCDs dispersed in the SnO<sub>2</sub>/NCDs/ZHS ternary nanohybrids, which increases the number of catalytically active sites *via* the close interfacial interaction.

BET measurements were carried out to investigate the physical properties of the ZHS and SnO<sub>2</sub>/NCDs/ZHS samples (Fig. S9†). As shown in Table S1,† pristine ZHS exhibited a BET surface area of 172.7 m<sup>2</sup> g<sup>-1</sup>, whereas that of SnO<sub>2</sub>/NCDs/ZHS was 105.6 m<sup>2</sup> g<sup>-1</sup>, defining a slit-like mesoporous structure with an average pore diameter around 2.5 nm (Fig. S9b†).<sup>31</sup> The decreased BET surface area in the SnO<sub>2</sub>/NCDs/ZHS is attributed to the jamming of partial pores by the numerous SnO<sub>2</sub> and NCDs hybridized *in situ* on the surface of ZHS. Therefore, the ZHS with a high BET surface area and mesoporous structure provided more surface adsorption sites and promoted mass transfer by the *in situ* loading of NCDs and SnO<sub>2</sub> on the surface of the mesoporous ZHS nanocube architecture (Scheme S1†).

### 3.2 Evaluation of photocatalytic activity under VIS-NIR irradiation

The efficiency evolution of NO conversion and toxic intermediate NO<sub>2</sub> formation over ZHS, SnO<sub>2</sub>/ZHS, NCDs/ZHS and SnO<sub>2</sub>/NCDs/ZHS samples was evaluated under visible-light irradiation. As shown in Fig. 3a, UV activation of pristine ZHS and SnO<sub>2</sub>/ZHS showed rather poor performances for NO removal under visible-light irradiation. After surface modification with NCDs, for the first 10 min NCDs/ZHS presented 23% NO conversion which decreased to 16% at 30 min, revealing that most of the photoinduced electrons on the NCDs recombined

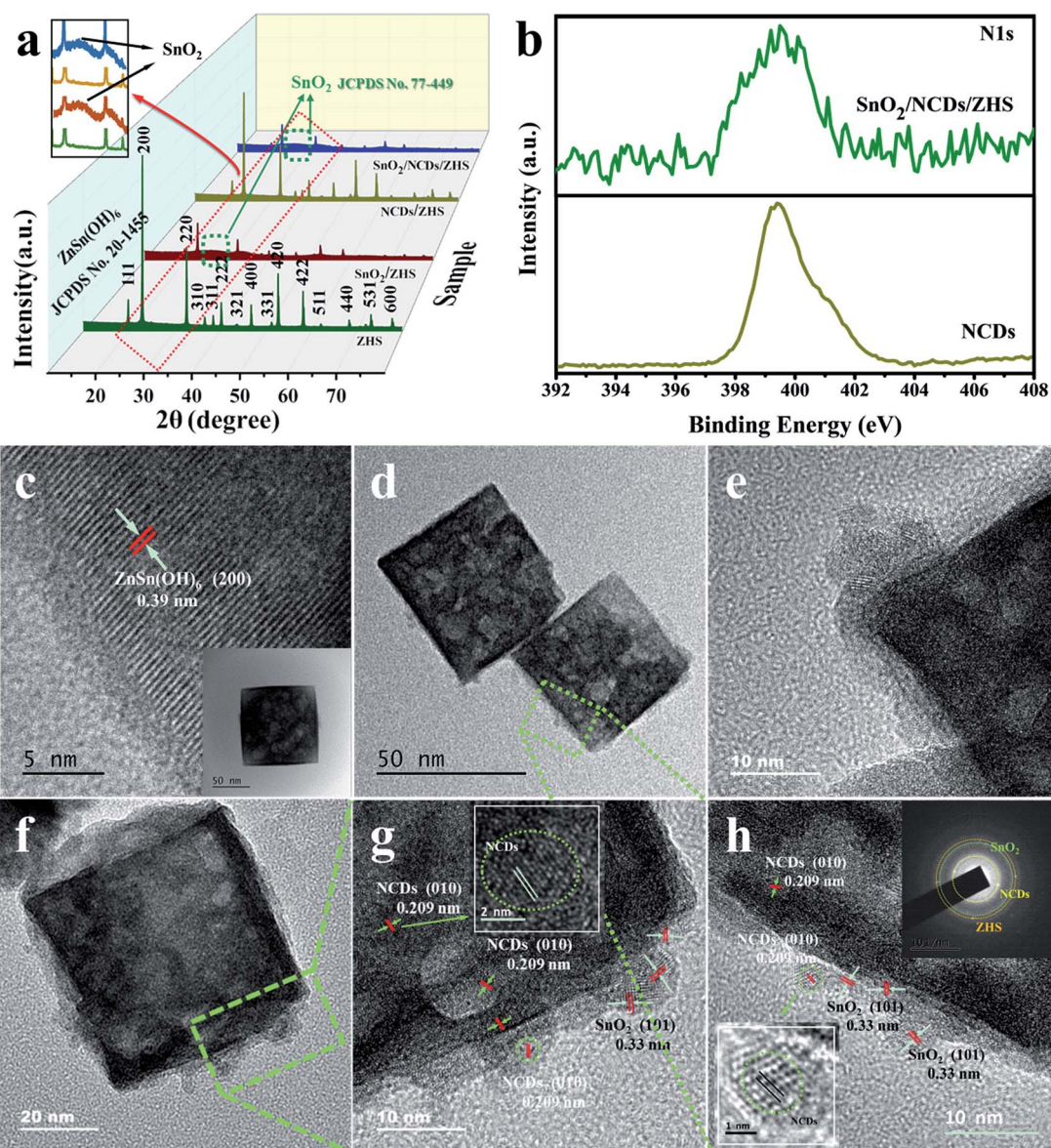


**Fig. 1** (a) XRD patterns of the as-prepared samples; (b) high-resolution XPS spectra of N 1s in NCDs and SnO<sub>2</sub>/NCDs/ZHS ternary nanohybrids; (c) TEM images of pristine ZHS; (d–h) TEM images and the corresponding selected area electron diffraction (SAED) patterns of the SnO<sub>2</sub>/NCDs/ZHS sample.

with the holes. Surprisingly, the NO conversion by the SnO<sub>2</sub>/NCDs/ZHS ternary nanohybrid under visible light was almost constant over the 30 min irradiation, and the value (37%) was apparently higher than the efficiency under simulated solar light irradiation (Fig. S10<sup>†</sup>). Meanwhile, the production of toxic intermediate NO<sub>2</sub> and catalyst deactivation were effectively suppressed. As expected, the constructed SnO<sub>2</sub>/NCDs/ZHS ternary nanohybrid showed significantly increased NO removal efficiency, above that of any single component or the binary counterparts.

Fig. 3b illustrates the durability of the SnO<sub>2</sub>/NCDs/ZHS sample during use. After 10 cycles, there was no distinct decrease of activity even after long and continued irradiation (375 min), while the selectivity for NO<sub>2</sub> was largely maintained (Fig. S11<sup>†</sup>). The thermal stability and composition structure

were also preserved after the 375 min stability tests with successive runs (Fig. S12–S14<sup>†</sup>). This superior performance of the SnO<sub>2</sub>/NCDs/ZHS photocatalyst was attributed to the persistently high selectivity of NO conversion to nitrate rather than to the toxic by-product NO<sub>2</sub>.

Moreover, photocatalytic activities of various samples for NO removal were investigated under UV, blue, green, red, and NIR lights (spectral composition of the light sources is shown in Fig. 3c). Fig. 3d illustrates the samples' capacity for destroying NO under lights of different wavelengths, with all samples kept in the dark and irradiated for 20 min. Firstly, there was no obvious activity from ZHS and SnO<sub>2</sub>/ZHS under VIS-NIR irradiation. Secondly, 13, 35, and 43 ppb of NO decomposed over NCDs/ZHS under the excitation of green, blue, and UV light, respectively. The visible-light induced activity of NCDs/ZHS was

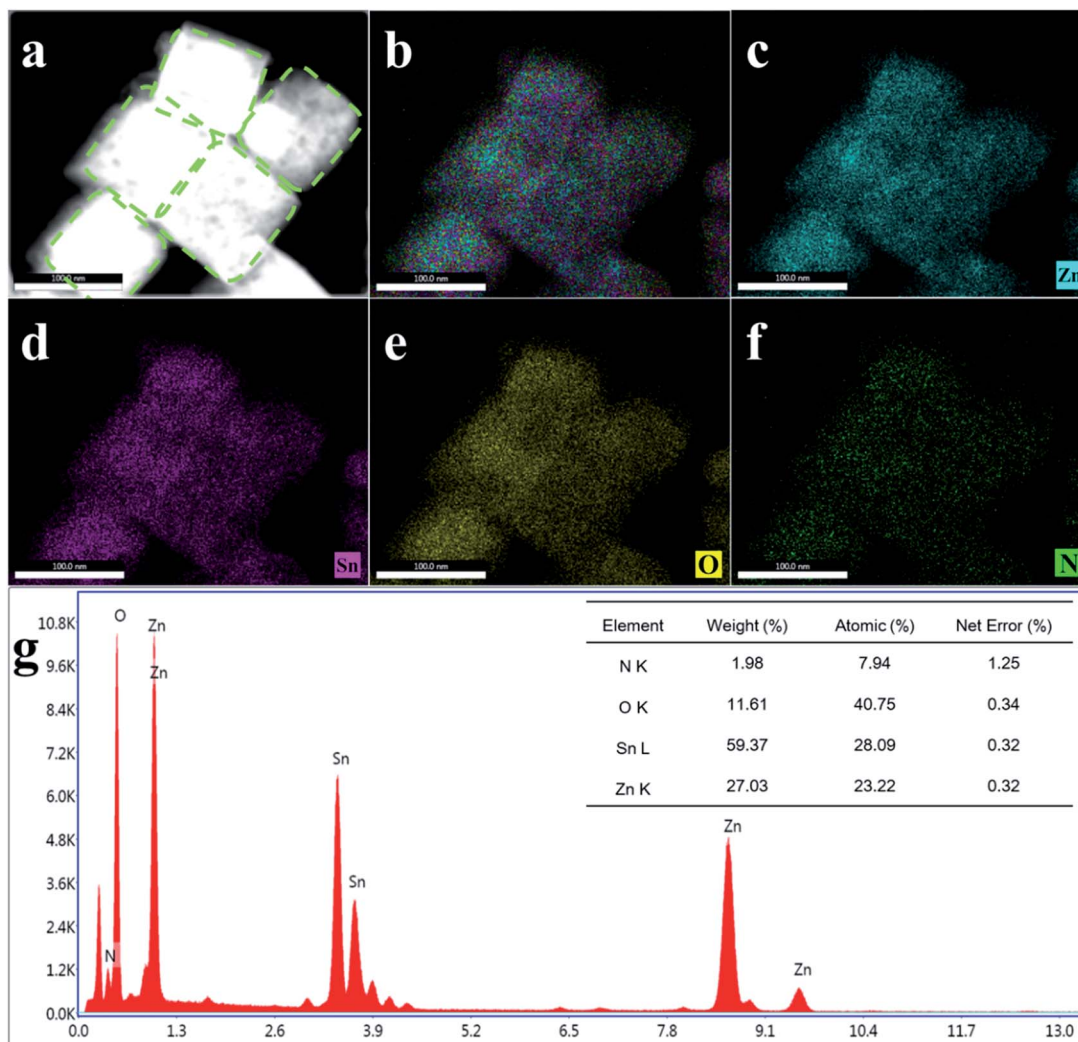


Fig. 2 (a) TEM image; (b–f) elemental mapping images of Zn, Sn, O and N; and (g) the corresponding EDS spectrum of SnO<sub>2</sub>/NCDs/ZHS nanohybrids.

mainly assigned to the excellent visible absorption of NCDs.<sup>32</sup> Under NIR light, 39 ppb of NO was decomposed by the SnO<sub>2</sub>/NCDs/ZHS ternary nanohybrid. This high NIR light-induced activity should be attributed to the synergistic effect of the SnO<sub>2</sub> cocatalyst and NCD up-conversion effect, since no corresponding performance was observed for either single component or the binary counterparts. Moreover, the photocatalytic activity of different samples at different wavelengths was investigated (Fig. 3e). It was shown that the synergistic effects and the stronger interfacial interaction in the SnO<sub>2</sub>/NCDs/ZHS ternary nanohybrid improved the broad-spectrum light absorption and redox ability, resulting in remarkably enhanced photocatalytic activity.

### 3.3 Optical and photoelectrochemical properties

To explain the superior performance of the SnO<sub>2</sub>/NCDs/ZHS ternary nanohybrid under VIS-NIR irradiation, the structure-activity relationship and oxygen activation mechanism were investigated in detail. Firstly, UV-Vis diffuse reflectance spectra

(DRS) were analyzed to study the light absorption of as-prepared photocatalysts. As shown in Fig. 4a, the absorption of pristine ZHS and the SnO<sub>2</sub>/ZHS binary composite was located in the UV region (200–350 nm),<sup>7</sup> indicating that UV activation of these samples offers no performance advantage under visible-light irradiation, which agrees with the results of NO removal (Fig. 3a). Notably, the optical absorption of the SnO<sub>2</sub>/NCDs/ZHS ternary nanohybrid dramatically increased in the VIS-NIR region after surface modification with NCDs. There are two absorption peaks centered at 240 and 350 nm, and they are ascribed to the  $\pi$ - $\pi^*$  transition of the C=C bond and the n- $\pi^*$  transition of the C=O bond, respectively.<sup>32</sup> Meanwhile, the expansion of absorption to 400–800 nm indirectly explains the resonance absorption peak of NCDs.<sup>33</sup> This result revealed that the introduction of NCDs obviously promotes the light absorption of SnO<sub>2</sub>/NCDs/ZHS nanohybrids.

The effect of introducing NCDs on the optical properties was also investigated by using a fluorescence spectrophotometer. Fig. 4b shows that NCDs exhibited distinct up-conversion fluorescence properties, with PL emission located at around

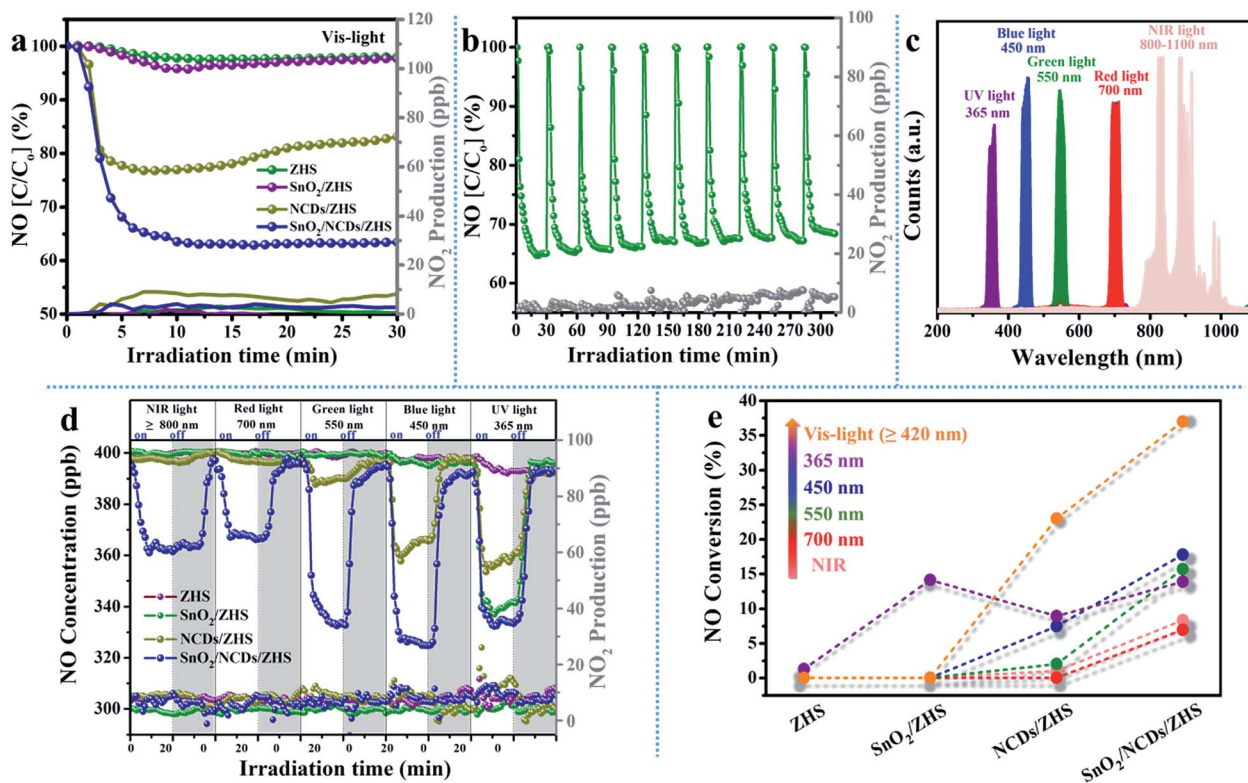


Fig. 3 (a) Time profiles of photocatalytic NO removal and the relative change of NO<sub>2</sub> over different photocatalysts under visible light ( $\lambda \geq 420$  nm) irradiation; (b) stability of the SnO<sub>2</sub>/NCDs/ZHS photocatalyst in 10 reaction cycles under visible light irradiation; (c) spectral composition of the different light sources; time dependence of NO removal activity (d) and the corresponding NO conversion ability (e) of ZHS, SnO<sub>2</sub>/ZHS, NCDs/ZHS and SnO<sub>2</sub>/NCDs/ZHS samples irradiated at different wavelengths.

UV (300–400 nm) and Vis (400–650 nm) regions after excitation at 550–850 nm.<sup>34</sup> This phenomenon shows that the introduced NCDs can convert light of long wavelengths to short wavelengths (even to UV light), resulting in efficient absorption of the fluorescence emitted from NCDs to produce charge carriers in the SnO<sub>2</sub>/NCDs/ZHS ternary nanohybrid.

To investigate the charge transfer efficiency, the surface photovoltage spectroscopy (SPS) analysis was used to reflect the carrier separation and transfer behavior under light irradiation.

In Fig. 5a, the pristine ZHS and the NCDs/ZHS composite showed no apparent surface photovoltage response, while SnO<sub>2</sub>/ZHS had a distinct response (8.5  $\mu$ A) in the UV range (300–375 nm).<sup>35</sup> For the SnO<sub>2</sub>/NCDs/ZHS nanohybrid, the strongest response (26  $\mu$ A) was obtained at 300–500 nm, suggesting more photo-induced charge transfer to the surface of the semiconductor.<sup>36</sup> This means that the charge separation of the SnO<sub>2</sub>/NCDs/ZHS ternary nanohybrid was improved by the introduction of the SnO<sub>2</sub> cocatalyst and NCDs.

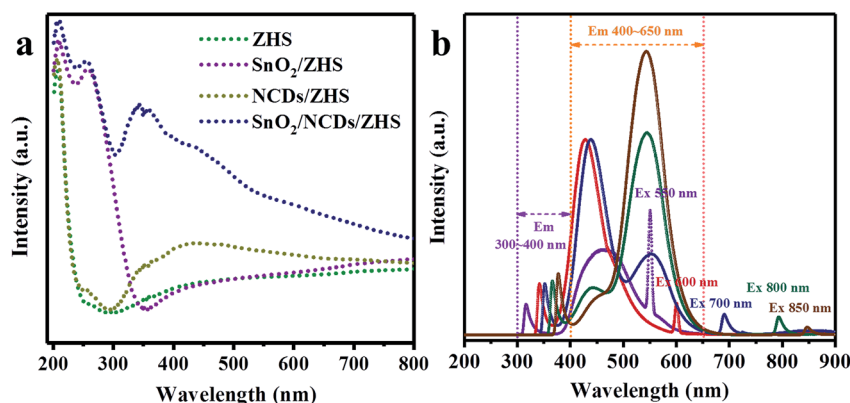


Fig. 4 (a) UV-vis diffuse reflectance spectra of ZHS, SnO<sub>2</sub>/ZHS, NCDs/ZHS and SnO<sub>2</sub>/NCDs/ZHS samples; (b) fluorescence spectra of NCDs with excitation of different wavelengths from 550 to 850 nm.

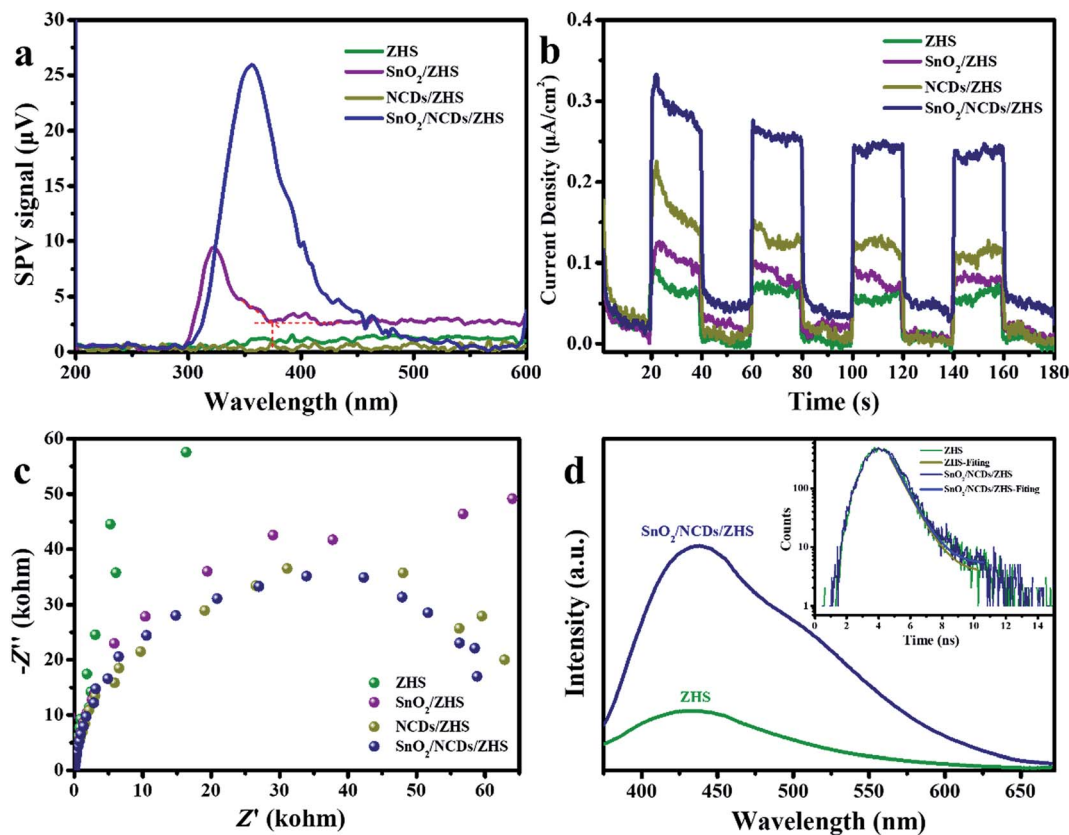


Fig. 5 Surface photovoltage spectroscopy, (b) transient photocurrent responses, (c) EIS Nyquist plots of ZHS, SnO<sub>2</sub>/ZHS, NCDs/ZHS and SnO<sub>2</sub>/NCDs/ZHS samples, and (d) photoluminescence spectra (inset: transient fluorescence decay spectra).

The transient photocurrent and electrochemical impedance spectra (EIS) of SnO<sub>2</sub>/NCDs/ZHS nanohybrid nanocubes were also measured and compared to those of pure samples and binary counterparts. Fig. 5b shows that pristine ZHS and SnO<sub>2</sub>/ZHS had a poor response, indicating a very low efficiency of photovoltaic conversion under visible-light irradiation. NCDs/ZHS exhibited a higher photocurrent density (0.22 μA cm<sup>-2</sup>), ascribed to the absorption of low-energy photons by NCDs.<sup>25</sup> In comparison, the SnO<sub>2</sub>/NCDs/ZHS nanohybrid exhibited the highest photocurrent response (0.34 μA cm<sup>-2</sup>) under visible-light irradiation, showing that the introduction of the SnO<sub>2</sub> cocatalyst synergistically promotes the separation and transfer of more electron-hole pairs on the interface.<sup>37</sup> Similar results were obtained by EIS (Fig. 5c), *i.e.*, the smallest Nyquist circle radius of SnO<sub>2</sub>/NCDs/ZHS revealed its lowest charge transfer barrier and excellent charge transfer efficiency.<sup>38</sup>

To further investigate the charge transfer dynamics of SnO<sub>2</sub>/NCDs/ZHS nanohybrids, photoluminescence spectra (PL) were recorded. As shown in Fig. 5d, a broad and strong PL peak appeared at around 380–650 nm, which was attributed to the recombination process of self-trapped excitation.<sup>23</sup> Compared with pristine ZHS, the PL intensity of SnO<sub>2</sub>/NCDs/ZHS increased distinctly, indicating that additional new recombination centers were created after surface modification with the SnO<sub>2</sub> cocatalyst and NCDs. However, the nanosecond-level time-resolved fluorescence decay spectra (inset in Fig. 5d) revealed

that the lifetime of photogenerated carriers over SnO<sub>2</sub>/NCDs/ZHS (τ = 0.82 ns) was longer than that of the pristine ZHS (τ = 0.78 ns), which implied that the influence of new recombination centers on the carrier lifetime can be ignored. As already proved by the above-mentioned consistent results from transient photocurrent, EIS, and SPS, the overall efficiency of photogenerated carrier separation and transfer was distinctly enhanced over the ternary SnO<sub>2</sub>/NCDs/ZHS nanohybrids. These phenomena implied that the interface formed in the SnO<sub>2</sub>/NCDs/ZHS ternary nanohybrid was favorable for effective electron-transfer quenching for SnO<sub>2</sub> in the excited state due to the Z-scheme mechanism. Thus, NCDs as an electron transport medium can rapidly capture and transfer electrons from photo-excited SnO<sub>2</sub> to ZHS. Holes and electrons accumulate in the valence band (VB) of SnO<sub>2</sub> and in the conduction band (CB) of ZHS, respectively. This results in the maximum redox capacity in the SnO<sub>2</sub>/NCDs/ZHS nanohybrid.<sup>39,40</sup> To prove the effect of the interfacial interaction on the electron transfer route, a mechanically mixed sample was prepared that contained ZHS/SnO<sub>2</sub> (SnO<sub>2</sub>, 12%) and 1.7 vol% NCDs, similar in composition to the SnO<sub>2</sub>/NCDs/ZHS components. The photocatalytic activity of the physically mixed samples was much lower (5%) than that of the SnO<sub>2</sub>/NCDs/ZHS Z-scheme nanohybrid (37%) under identical conditions, indicating that the high interfacial contact efficiency played an important role in the photocatalytic properties (Fig. S15†).

Based on all the above results, we propose a hypothetical charge transfer route for the Z-scheme-type photocatalyst of the SnO<sub>2</sub>/NCDs/ZHS ternary nanohybrid, as evidenced by transient photocurrent, EIS, PL and SPS results.<sup>41</sup> Appropriate amounts of SnO<sub>2</sub> cocatalyst and the “bridge” of NCDs can synergistically facilitate the spatial separation and migration of interfacial photoinduced electrons, thus effectively improving the photocatalytic performance.

### 3.4 ROS identification and separation/transfer pathways of charge carriers

In order to elucidate the mechanism of reactive radical production, the generation of free hydroxyl ( $\cdot\text{OH}$ ) and superoxide ( $\cdot\text{O}_2^-$ ) radicals from pristine ZHS, NCDs/SnO<sub>2</sub>, NCDs/ZHS

and SnO<sub>2</sub>/NCDs/ZHS samples was measured under visible-light irradiation.<sup>42</sup> As elucidated in Fig. 6a, signals assigned to  $\cdot\text{OH}$  and  $\cdot\text{O}_2^-$  radicals were clearly observed in the SnO<sub>2</sub>/NCDs/ZHS Z-scheme system and their intensities increased with irradiation time, while no apparent signals were detected for pristine ZHS under identical conditions (Fig. S16†). As a result, the main reactive oxygen species (ROS) for the SnO<sub>2</sub>/NCDs/ZHS Z-scheme nanohybrid were  $\cdot\text{OH}$  and  $\cdot\text{O}_2^-$  radicals during the photocatalytic reaction, guaranteeing high selectivity of the photocatalyst. However, in Fig. S17† under the same conditions, the DMPO- $\cdot\text{OH}$  signals were detected only for NCDs/SnO<sub>2</sub> but not for NCDs/ZHS. Meanwhile, apparent signals of  $\cdot\text{O}_2^-$  radicals only appeared for NCDs/ZHS under visible-light irradiation. The significant difference in ROS generation implies that the construction of the SnO<sub>2</sub>/NCDs/ZHS ternary Z-scheme

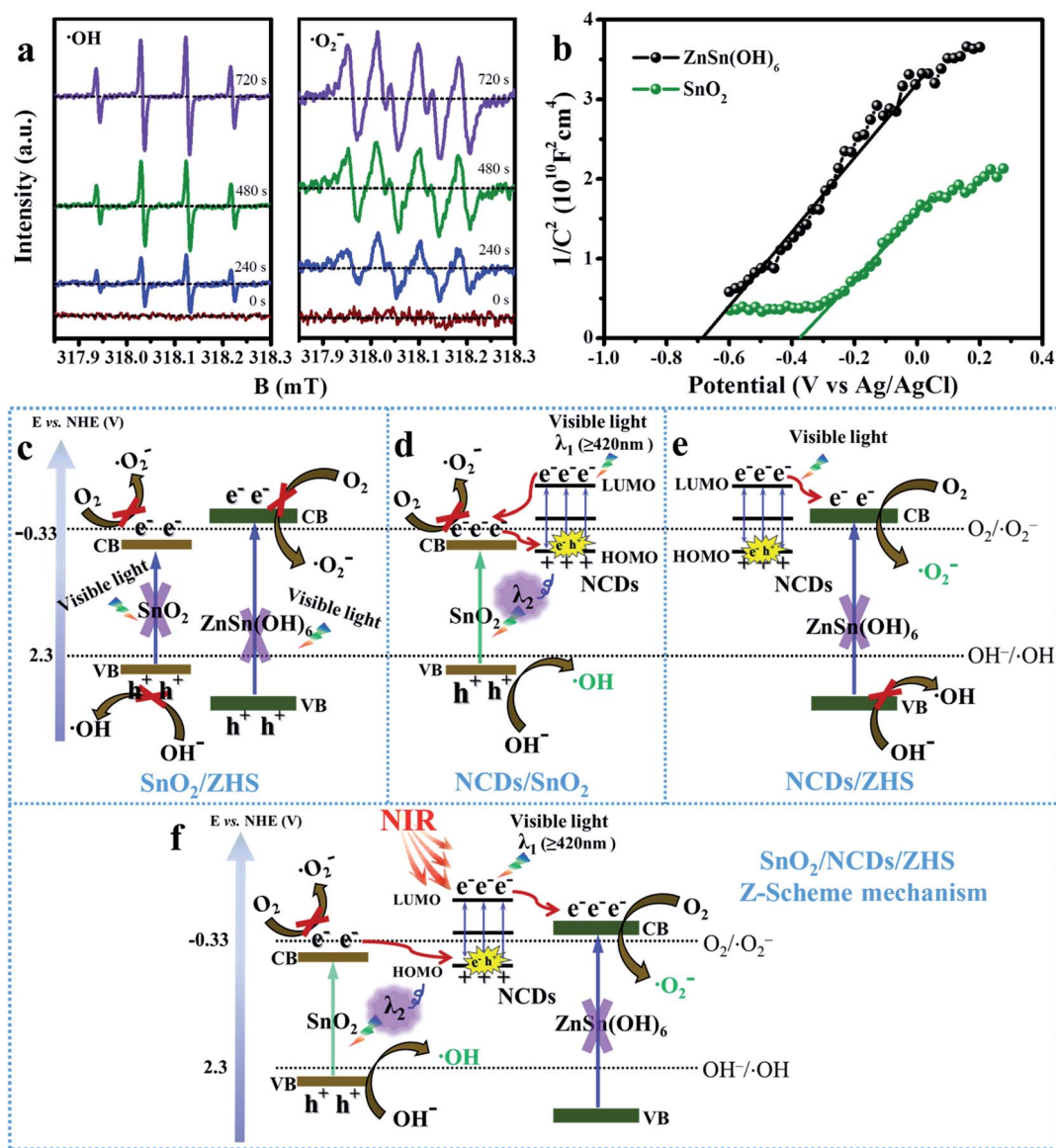


Fig. 6 (a) Room-temperature ESR spectra of SnO<sub>2</sub>/NCDs/ZHS nanohybrids for  $\cdot\text{O}_2^-$  and  $\cdot\text{OH}$  during 12 min VIS-light irradiation, using DMPO as the spin trapping agent; (b) Mott-Schottky plots of as-prepared ZHS and SnO<sub>2</sub> in 0.5 M Na<sub>2</sub>SO<sub>4</sub> aqueous solution (pH = 7.0); the energy level diagram and charge transfer route of SnO<sub>2</sub>/ZHS (c), NCDs/ZHS (d), NCDs/SnO<sub>2</sub> (e) and SnO<sub>2</sub>/NCDs/ZHS (f).

nanohybrid changed the transfer pathway of photoelectrons and maximized the redox capacity under VIS-NIR irradiation.

To further confirm our hypothesis, the energy level diagram was both calculated and measured. From the UV-Vis diffuse reflectance spectra of as-prepared samples (Fig. S18†), the Tauc plots of as-prepared ZHS, SnO<sub>2</sub> and NCDs/SnO<sub>2</sub>/ZHS are shown in Fig. S19.† Then the optical band gaps were estimated as 5.68 eV for ZHS and 3.27 eV for SnO<sub>2</sub>.<sup>43</sup> Mott-Schottky (M-S) plotting was also used to obtain the CB position of the semiconductor. Fig. 6b shows that the flat band potentials are -0.68 and -0.36 V vs. Ag/AgCl at pH 7.<sup>44</sup> Thus, the respective CB positions of ZHS and SnO<sub>2</sub> were estimated to be -0.48 and -0.16 V through the Nernst equation.<sup>45</sup> Combined with the bandgap results, the VB tops of ZHS and SnO<sub>2</sub> were calculated to be 5.20 and 3.11 V, respectively, suggesting that the band gap energies only allow ZHS and SnO<sub>2</sub> to be excited under UV light (Fig. 6c).<sup>43</sup> As shown in Fig. 4a and b, the introduction of NCDs triggered the DRS of the SnO<sub>2</sub>/NCDs/ZHS ternary nanohybrid, with a good overlap with the emission peaks in the PL spectrum. This phenomenon indicated that SnO<sub>2</sub>/NCDs/ZHS could efficiently absorb the fluorescence emitted from NCDs, allowing the excitation of SnO<sub>2</sub> under VIS-NIR illumination to produce ROS (Fig. 6d and S20†). Moreover, NCDs as light-trapping centers can effectively absorb low-energy photons to produce photoinduced electrons, which can rapidly transfer to the CB of ZHS to generate  $\cdot\text{O}_2^-$  radicals (Fig. 6e and S17b†).<sup>25</sup> The NCD amount loaded in each sample was evaluated by the elemental analysis (Table S2 and Fig. S21†). The results showed that the activities of NCDs/ZHS nanocomposites with different amounts of NCD precursor inserted are similar (Fig. S22†). The higher activity in SnO<sub>2</sub>/NCDs/ZHS was due to the Z-scheme mechanism. This behavior indicated that the loading of NCDs and the SnO<sub>2</sub> cocatalyst in the SnO<sub>2</sub>/NCDs/ZHS ternary nanohybrid can enhance the quantum efficiency and redox ability to improve the photocatalytic activity (Fig. S23 and S24†).

Firstly, the strong signals of  $\cdot\text{OH}$  radicals are attributed to the restructured holes in the VB of the SnO<sub>2</sub> cocatalyst. The holes can oxidize OH<sup>-</sup> into  $\cdot\text{OH}$  radicals that can in turn oxidize the target pollutants of NO. However, the CB edge of SnO<sub>2</sub> is located at -0.16 V (vs. NHE), which is more positive than the redox potential of O<sub>2</sub>/ $\cdot\text{O}_2^-$  (-0.33 V vs. NHE).<sup>46</sup> Thus, O<sub>2</sub> cannot be directly reduced to  $\cdot\text{O}_2^-$  by the SnO<sub>2</sub> cocatalyst. The useless electrons in the CB of SnO<sub>2</sub> are transferred to NCDs and recombine with holes to improve the charge separation, which enhances the efficient mass of electrons and holes. Meanwhile, the NCDs can absorb VIS-NIR light and generate photoinduced electrons that can rapidly transfer to ZHS. The CB edge of ZHS is concentrated near -0.48 V (vs. NHE), a potential that is more negative than the redox potential of O<sub>2</sub>/ $\cdot\text{O}_2^-$ , resulting in the generation of  $\cdot\text{O}_2^-$  radicals to remove NO. On the basis of these results, a likely charge transfer route of ternary SnO<sub>2</sub>/NCDs/ZHS Z-scheme nanohybrids is proposed and shown in Fig. 6f. This high-efficiency spatial charge transfer *via* the Z-scheme mechanism gains the maximum redox ability for the nanohybrids by increasing the effective mass of electrons on ZHS and that of holes on SnO<sub>2</sub>, resulting in efficient and sustainable generation

of  $\cdot\text{OH}$  and  $\cdot\text{O}_2^-$ . As a result, the solar light utilization efficiency and photocatalytic performance can be effectively improved.

### 3.5 Analysis of intermediates and the photocatalytic NO oxidation mechanism

To understand the pathway of photocatalytic NO removal, *in situ* DRIFTS was employed to check the possible reaction intermediates and products on the photocatalyst surface in a special reaction cell (Fig. 7a and Scheme S2†). IR spectra were recorded during the adsorption process in the dark and photocatalytic reaction under visible light irradiation. Nitro compounds were adsorbed on the surface of the mesoporous SnO<sub>2</sub>/NCDs/ZHS nanohybrid, as shown in Fig. S25.† Major absorption bands of SnO<sub>2</sub>/NCDs/ZHS are concentrated at monodentate nitrates (1540, 1288 and 1060–1010 cm<sup>-1</sup>)<sup>47,48</sup> and bidentate nitrites (1392 and 1125 cm<sup>-1</sup>)<sup>49</sup> and (1250 and 1085 cm<sup>-1</sup>).<sup>47</sup> Compared with ZHS and binary SnO<sub>2</sub>/ZHS (Fig. S26 and S27†), new absorption bands appeared at 1800 to 1600 cm<sup>-1</sup>, and were assigned to the typical combination band associated with NO and free nitrate.<sup>50</sup> Thus, the SnO<sub>2</sub>/NCDs/ZHS Z-scheme nanohybrid has more active sites due to the loading of NCDs (Fig. S28†). Constructing the ternary SnO<sub>2</sub>/NCDs/ZHS nanohybrid promotes the formation of new active centers to facilitate the adsorption and activation of NO, effectively promoting its conversion to the final products.

Once visible light was applied to initiate the photocatalytic reaction, a set of obvious bands can be observed in the IR spectra (Fig. 7b). First, the band at 3720 cm<sup>-1</sup> was assigned to the surface free OH resulting from ZHS after visible-light illumination, and these free OH can migrate to the surface of SnO<sub>2</sub>.<sup>47</sup> The surface structure and other information on SnO<sub>2</sub>/NCDs/ZHS further illustrated the characteristic surface parts rich in O-H, which favored the production of highly reactive oxygen radicals to accelerate oxygen activation (Fig. S3†).<sup>7</sup> This implies that mesoporous ZHS can supply a sufficient amount of free surface OH to SnO<sub>2</sub> for the generation of hydroxyl radicals (Fig. 6a). Second, a new absorption band appeared at 2208 cm<sup>-1</sup>, and can be ascribed to electrons from the adsorbed NO being trapped by the photogenerated holes and then converted into NO<sup>+</sup>.<sup>51,52</sup> The production of free NO<sup>+</sup> ions enhanced the activation and conversion of NO on the SnO<sub>2</sub>/NCDs/ZHS Z-scheme nanohybrids. Finally, the activated NO was immediately transformed into other nitrogen species. The accumulated monodentate nitrates (1500–1440 and 1040–1010 cm<sup>-1</sup>)<sup>53,54</sup> and bidentate nitrites (1340–1330 and 1120–1060 cm<sup>-1</sup>)<sup>54–56</sup> immediately appeared and their amounts gradually increased after 30 min illumination. Sharp bands at 1750 and 1240 cm<sup>-1</sup> were assigned to bidentate nitrates.<sup>57,58</sup> Notably, with increase in IR absorbance intensity of NO<sub>2</sub><sup>-</sup> and NO<sub>3</sub><sup>-</sup> species, the cumulative final products increase, illustrating the efficient and sustainable generation of  $\cdot\text{OH}$  and  $\cdot\text{O}_2^-$  radicals to remove NO. Both  $\cdot\text{OH}$  and  $\cdot\text{O}_2^-$  radicals were involved in the photocatalytic oxidation reactions realized by the Z-scheme mechanism (Fig. 6f). However, the intensities of NO<sup>+</sup> free ions and surface free OH have no clear rise along with the increase of irradiation and reaction time. This phenomenon demonstrates that the

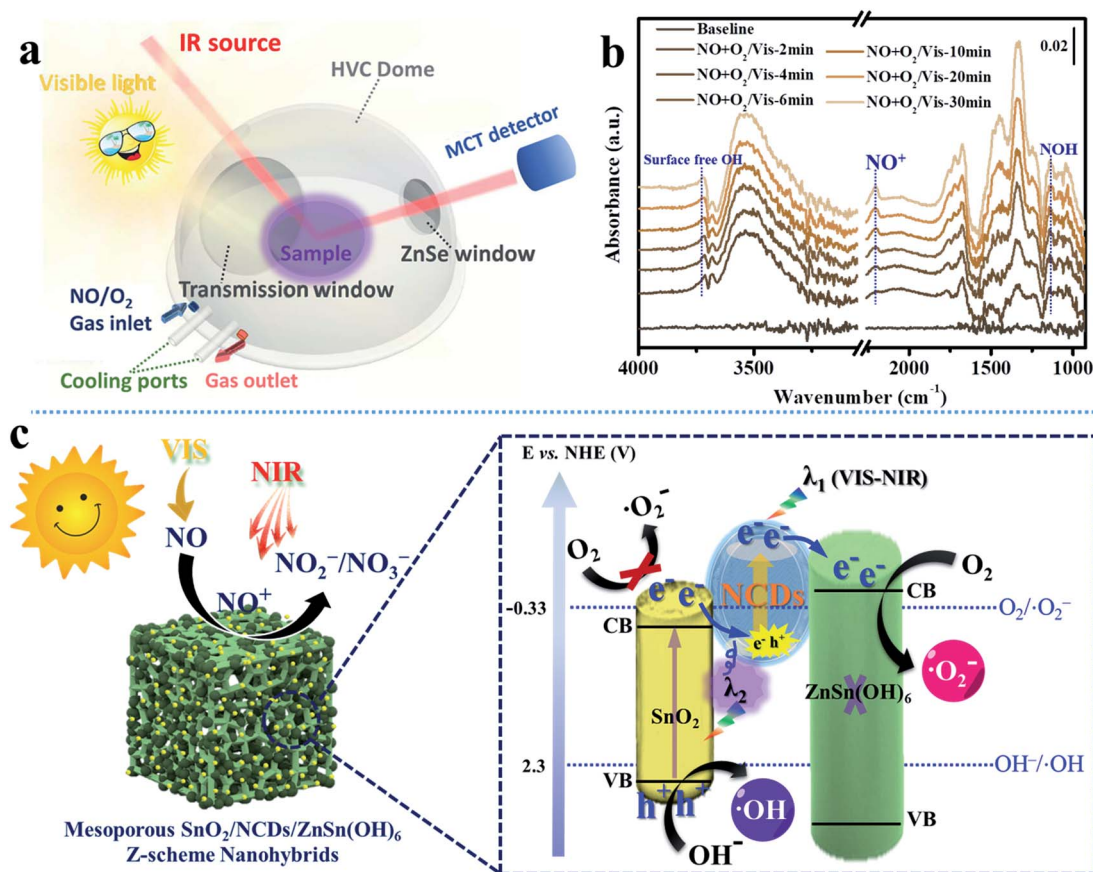


Fig. 7 (a) Schematic illustration of the reaction cell for the *in situ* DRIFTS study; (b) *in situ* IR spectra of the SnO<sub>2</sub>/NCDs/ZHS Z-scheme photocatalyst during photocatalytic NO oxidation under visible light irradiation; (c) pathway of photocatalytic NO transformation and the reaction mechanism on the surface of the SnO<sub>2</sub>/NCDs/ZHS Z-scheme nanohybrid under VIS-NIR irradiation.

intermediate of NO<sup>+</sup> and active species of surface free OH can be continuously produced and consumed during the photocatalytic reaction. This phenomenon demonstrated that dilute NO can be activated and converted to stable final products of nitrite/nitrate radicals (NO → NO<sup>+</sup> → NO<sub>2</sub><sup>-</sup>/NO<sub>3</sub><sup>-</sup>) by the abundant photo-generated reactive species (Fig. 7c). The accumulated amounts of NO<sub>2</sub><sup>-</sup> and NO<sub>3</sub><sup>-</sup> on the surfaces of the SnO<sub>2</sub>/NCDs/ZHS were determined by the ion chromatography (IC) method (Fig. S29<sup>†</sup>). The amount of NO<sub>3</sub><sup>-</sup> is higher than the generation of NO<sub>2</sub><sup>-</sup>. This phenomenon shows that most of the NO was completely oxidized to NO<sub>3</sub><sup>-</sup>. These results provide accurate evidence of major NO transformation over SnO<sub>2</sub>/NCDs/ZHS. Based on these results, a mechanism of photocatalytic NO oxidation by the SnO<sub>2</sub>/NCDs/ZHS Z-scheme nanohybrid was proposed and is shown in eqn (1)–(4). This work provides deep insight into the mechanism of spatial charge transfer in constructing Z-scheme composites, and demonstrates the maximum redox capacity of the composite in transforming NO to harmless final products while restraining the production of toxic intermediates *via* wide-spectrum VIS-NIR photocatalysis.



## 4. Conclusions

In summary, we have successfully developed a facile *in situ* solvothermal method to construct a ternary SnO<sub>2</sub>/NCDs/ZHS Z-scheme nanohybrid. The prepared material showed VIS-NIR absorption due to the highly dispersed NCDs with the up-conversion effect, resulting in two distinctive excitation routes for the photoinduced electrons. The formed structure facilitates the synergetic transfer of photoinduced carriers in the SnO<sub>2</sub>/NCDs/ZHS ternary nanohybrid *via* a Z-scheme-type mechanism, eliminating the charge transfer barrier and increasing the efficient mass of electrons and holes. The constructed ternary SnO<sub>2</sub>/NCDs/ZHS Z-scheme nanohybrid facilitated the redox interaction to accelerate oxygen activation and maximized the redox capacity of the nanohybrids, resulting in a remarkable enhancement in NO removal efficiency and high NO<sub>2</sub> selectivity under VIS-NIR irradiation. Cycling experiments and *in situ* DRIFTS results also confirmed the reusability and stability of the prepared photocatalysts for removing NO from gases and

illustrated the reaction pathway. Overall, the SnO<sub>2</sub>/NCDs/ZHS Z-scheme photocatalyst can efficiently transform NO into harmless final products and suppress toxic intermediates. More generally, this work indicates an effective strategy to design photocatalytic nanomaterials with strong redox capacity, high selectivity and wide-range absorption for environmental remediation.

## Conflicts of interest

There are no conflicts to declare.

## Acknowledgements

This research was financially supported by the National Key Research and Development Program of China (2016YFA0203000 and 2017YFC0212200) and the National Science Foundation of China (No. 41573138 and No. 51878644). Moreover, we acknowledge the partial support by the Key Research and Development Program of Shaanxi Province (No. 2018ZDCXL-SF-02-04). Yu Huang was also supported by the "Hundred Talent Program" of the Chinese Academy of Sciences.

## References

- H. Li, X. Yan, B. Lin, M. Xia, J. Wei, B. Yang and G. Yang, *Nano Energy*, 2018, **47**, 481–493.
- H. Li, J. Shang, Z. Ai and L. Zhang, *J. Am. Chem. Soc.*, 2015, **137**, 6393–6399.
- J. T. Lin, M. B. McElroy and K. F. Boersma, *Atmos. Chem. Phys.*, 2010, **10**, 63–78.
- G. Dong, L. Yang, F. Wang, L. Zang and C. Wang, *ACS Catal.*, 2016, **6**, 6511–6519.
- Q. Zhang, D. Q. Lima, I. Lee, F. Zaera, M. Chi and Y. Yin, *Angew. Chem., Int. Ed.*, 2011, **50**, 7088–7092.
- Z. Luo, T. Wang, J. Zhang, C. Li, H. Li and J. Gong, *Angew. Chem., Int. Ed.*, 2017, **56**, 12878–12882.
- X. Fu, J. Wang, D. Huang, S. Meng, Z. Zhang, L. Li, T. Miao and S. Chen, *ACS Catal.*, 2016, **6**, 957–968.
- Y. Chen, D. Li, M. He, Y. Hu, H. Ruan, Y. Lin, J. Hu, Y. Zheng and Y. Shao, *Appl. Catal., B*, 2012, **113–114**, 134–140.
- L. Han, J. Liu, Z. Wang, K. Zhang, H. Luo, B. Xu, X. Zou, X. Zheng, B. Ye and X. Yu, *CrystEngComm*, 2012, **14**, 3380–3386.
- J. Yin, F. Gao, C. Wei and Q. Lu, *Inorg. Chem.*, 2012, **51**, 10990–10995.
- C. Chen, X. Zheng, J. Yang and M. Wei, *Phys. Chem. Chem. Phys.*, 2014, **16**, 20073–20078.
- X. Fu, X. Wang, Z. Ding, D. Y. C. Leung, Z. Zhang, J. Long, W. Zhang, Z. Li and X. Fu, *Appl. Catal., B*, 2009, **91**, 67–72.
- H. Wang, X. Yuan, Y. Wu, G. Zeng, W. Tu, C. Sheng, Y. Deng, F. Chen and J. W. Chew, *Appl. Catal., B*, 2017, **209**, 543–553.
- X. Fu, D. Huang, Y. Qin, L. Li, X. Jiang and S. Chen, *Appl. Catal., B*, 2014, **148–149**, 532–542.
- L. Wang, K. Tang, Z. Liu, D. Wang, J. Sheng and W. Cheng, *J. Mater. Chem.*, 2011, **21**, 4352–4357.
- J. M. Wu and Y. N. Chen, *Dalton Trans.*, 2015, **44**, 16294–16303.
- W. H. Feng, Z. X. Pei, Z. B. Fang, M. L. Huang, M. L. Lu, S. X. Weng, Z. Y. Zheng, J. Hu and P. Liu, *J. Mater. Chem. A*, 2014, **2**, 7802–7811.
- H. Li, Y. Cui, W. Hong and B. Xu, *Chem. Eng. J.*, 2013, **228**, 1110–1120.
- Y. Huang, W. Wang, Q. Zhang, J.-j. Cao, R.-j. Huang, W. Ho and S. C. Lee, *Sci. Rep.*, 2016, **6**, 23435.
- H. Li, W. Tu, Y. Zhou and Z. Zou, *Adv. Sci.*, 2016, **3**, 1500389.
- Y. Jia, S. Li, J. Gao, G. Zhu, F. Zhang, X. Shi, Y. Huang and C. Liu, *Appl. Catal., B*, 2019, **240**, 241–252.
- L. Tang, C. Feng, Y. Deng, G. Zeng, J. Wang, Y. Liu, H. Feng and J. Wang, *Appl. Catal., B*, 2018, **230**, 102–114.
- Y. Li, X. Wu, J. Li, K. Wang and G. Zhang, *Appl. Catal., B*, 2018, **229**, 218–226.
- S. Sun, T. Hisatomi, Q. Wang, S. Chen, G. Ma, J. Liu, S. Nandy, T. Minegishi, M. Katayama and K. Domen, *ACS Catal.*, 2018, **8**, 1690–1696.
- Y.-Q. Zhang, D.-K. Ma, Y.-G. Zhang, W. Chen and S.-M. Huang, *Nano Energy*, 2013, **2**, 545–552.
- N. C. T. Martins, J. Angelo, A. V. Girao, T. Trindade, L. Andrade and A. Mendes, *Appl. Catal., B*, 2016, **193**, 67–74.
- F. Wang, Y. Wu, Y. Wang, J. Li, X. Jin, Q. Zhang, R. Li, S. Yan, H. Liu, Y. Feng, G. Liu and W. Lv, *Chem. Eng. J.*, 2019, **356**, 857–868.
- J. M. Wu and Y. N. Chen, *Dalton Trans.*, 2015, **44**, 16294–16303.
- H. Zhang, H. Huang, H. Ming, H. Li, L. Zhang, Y. Liu and Z. Kang, *J. Mater. Chem.*, 2012, **22**, 10501–10506.
- X. Mao, R. Zhou, S. Zhang, L. Ding, L. Wan, S. Qin, Z. Chen, J. Xu and S. Miao, *Sci. Rep.*, 2016, **6**, 19390.
- C. Xue, H. Li, H. An, B. Yang, J. Wei and G. Yang, *ACS Catal.*, 2018, **8**, 1532–1545.
- J. Zhang, X. Zhang, S. Dong, X. Zhou and S. Dong, *J. Photochem. Photobiol., A*, 2016, **325**, 104–110.
- H. Wang, P. Sun, S. Cong, J. Wu, L. Gao, Y. Wang, X. Dai, Q. Yi and G. Zou, *Nanoscale Res. Lett.*, 2016, **11**, 27.
- J. Tian, Y. Leng, Z. Zhao, Y. Xia, Y. Sang, P. Hao, J. Zhan, M. Li and H. Liu, *Nano Energy*, 2015, **11**, 419–427.
- L. J. Zhang, S. Li, B. K. Liu, D. J. Wang and T. F. Xie, *ACS Catal.*, 2014, **4**, 3724–3729.
- D. Gross, I. Mora-Sero, T. Dittrich, A. Belaidi, C. Mauser, A. J. Houtepen, E. Da Como, A. L. Rogach and J. Feldmann, *J. Am. Chem. Soc.*, 2010, **132**, 5981–5983.
- G. Dong, L. Zhao, X. Wu, M. Zhu and F. Wang, *Appl. Catal., B*, 2019, **245**, 459–468.
- Y. Lu, Y. Huang, Y. Zhang, J.-j. Cao, H. Li, C. Bian and S. C. Lee, *Appl. Catal., B*, 2018, **231**, 357–367.
- Z.-F. Huang, J. Song, X. Wang, L. Pan, K. Li, X. Zhang, L. Wang and J.-J. Zou, *Nano Energy*, 2017, **40**, 308–316.
- K. Maeda, *ACS Catal.*, 2013, **3**, 1486–1503.
- C. Kim, K. M. Cho, A. Al-Saggaf, I. Gereige and H.-T. Jung, *ACS Catal.*, 2018, **8**, 4170–4177.
- Y. Huang, P. Wang, Z. Wang, Y. Rao, J.-j. Cao, W. Ho and S. C. Lee, *Appl. Catal., B*, 2018, **240**, 122–131.

- 43 J. Tauc, R. Grigorovici and A. Vancu, *Phys. Status Solidi B*, 1966, **15**, 627–637.
- 44 M. Curti, A. Kirsch, L. I. Granone, F. Tarasi, G. López-Robledo, D. W. Bahnemann, M. M. Murshed, T. M. Gesing and C. B. Mendive, *ACS Catal.*, 2018, **8**, 8844–8855.
- 45 J. Swaminathan, R. Subbiah and V. Singaram, *ACS Catal.*, 2016, **6**, 2222–2229.
- 46 G. Zhu, M. Hojamberdiev, S. Zhang, S. T. U. Din and W. Yang, *Appl. Surf. Sci.*, 2019, **467–468**, 968–978.
- 47 J. C. S. Wu and Y. T. Cheng, *J. Catal.*, 2006, **237**, 393–404.
- 48 Y. Zhou, Z. Zhao, F. Wang, K. Cao, D. E. Doronkin, F. Dong and J.-D. Grunwaldt, *J. Hazard. Mater.*, 2016, **307**, 163–172.
- 49 K. Hadjiivanov, V. Avreyska, D. Klissurski and T. Marinova, *Langmuir*, 2002, **18**, 1619–1625.
- 50 H. Li, H. Shang, X. Cao, Z. Yang, Z. Ai and L. Zhang, *Environ. Sci. Technol.*, 2018, **52**, 8659–8665.
- 51 H. Wang, Y. Sun, G. Jiang, Y. Zhang, H. Huang, Z. Wu, S. C. Lee and F. Dong, *Environ. Sci. Technol.*, 2018, **52**, 1479–1487.
- 52 W. Cui, J. Li, F. Dong, Y. Sun, G. Jiang, W. Cen, S. C. Lee and Z. Wu, *Environ. Sci. Technol.*, 2017, **51**, 10682–10690.
- 53 H. Y. Huang and R. T. Yang, *Langmuir*, 2001, **17**, 4997–5003.
- 54 X. Li, Y. Sun, T. Xiong, G. Jiang, Y. Zhang, Z. Wu and F. Dong, *J. Catal.*, 2017, **352**, 102–112.
- 55 W. Cui, J. Li, W. Cen, Y. Sun, S. C. Lee and F. Dong, *J. Catal.*, 2017, **352**, 351–360.
- 56 K. I. Hadjiivanov, *Catal. Rev.*, 2000, **42**, 71–144.
- 57 M. Kantcheva and E. Z. Ciftlikli, *J. Phys. Chem. B*, 2002, **106**, 3941–3949.
- 58 T. J. Toops, D. B. Smith and W. P. Partridge, *Appl. Catal., B*, 2005, **58**, 245–254.